OPTICAL TOMOGRAPHY

Three-dimensional representation of late-arriving photons for detecting inhomogeneities in diffuse optical tomography

A.Yu. Potlov, S.G. Proskurin, S.V. Frolov

Abstract. **A method for rapid detection of absorbing inhomogeneity in a strongly scattering medium having the properties of a biological tissue before the image reconstruction is described based on the principles of diffuse optical tomography. The method is based on preliminary processing of a three-dimensional surface obtained from the set of time-resolved data in the Cartesian coordinate system, followed by its conformal transformation into two surfaces in the cylindrical coordinate system. A specific feature of the method is the use of late-arriving photons, scattered and diffusely transmitted through an optically turbid object.**

1. Introduction

Diffuse optical tomography (DOT) is a set of methods for studying biological tissues to the depth of 10–15 cm, based on extracting the information from the strongly scattered (diffuse) component of probing radiation [1–3]. With respect to the key characteristic – the type of probing radiation, the DOT methods are usually divided into three large groups, namely, the pulsed ones (time-resolved or time-of-flight optical tomography), the amplitude-modulated ones (frequency domain optical tomography), and the continuous ones (cw optical tomography). Besides, DOT is often combined with other diagnostic methods, e.g., with laser fluorescent diagnostics (diffuse fluorescence tomography).

It is important to note, that in a number of cases, DOT can replace the X-ray computed tomography (CT) and the magnetic resonance tomography (MRT), and sometimes it can be used as a complementary diagnostic method. In the process of CT and MRT examinations the patient has to stay immobile during a long time, which gives rise to additional problems in diagnostics of new-born and prematurely born infants. Their examination has to be performed under the twilight anaesthesia, which is not always acceptable and can give rise to additional complications. The DOT allows diagnostics of haematomas, tumours, brain cysts, including those in neonates [4]; in this case the optical waveguides are painlessly attached to the patient's head and he can move free enough.

A.Yu. Potlov, S.G. Proskurin, S.V. Frolov Tambov State Technical University, ul. Sovetskaya 106, 392000 Tambov, Russia; e-mail: zerner@yandex.ru

The existing methods of two- and three-dimensional medical imaging, including DOT, require a large RAM and a considerable computation rate of computer systems. While for solving most problems the required RAM can be easily provided by adding memory units to the existing system, the speed of a computing unit (processor core) has a definite limit [5]. This problem is solved by performing the calculations using graphics processors, which essentially increases the processing power. The technology of general-purpose graphics processing units (GPGPUs), i.e., using graphics processors for calculations, usually performed by the central processor unit, is rather new, the first 'open' codes having become available in the beginning of 2007 [5]. That is why in the present paper particular attention is paid to the possibility of direct detection of optical inhomogeneities without solving the inverse problem, i.e., in real-time regime, and, therefore, without the necessity of high-performance computer calculations.

The visualisation of a set of time-dependent point spread functions (TPSFs) in the form of a three-dimensional surface in the Cartesian coordinate system, proposed for time-resolved DOT in Ref. [6], allows inhomogeneities to be registered by observing the valleys in the corresponding parts of the resulting three-dimensional surfaces. Such an approach is simple and reliable; however, at the present stage it is applicable only to sufficiently large and strongly absorbing inhomogeneities. This is because in the image there is no unambiguous intensity level of the pulsed IR radiation, diffusely passed through the object and detected for different angles with high temporal resolution (less than 20 ps) that could allow unique differentiation between homogeneous and inhomogeneous cases.

The aim of the present paper is to improve the efficiency of direct detection of inhomogeneities in DOT, preceding the solution of the inverse problem, at the expense of a conformal transformation of TPSF surfaces from the Cartesian to the cylindrical coordinate system in homogeneous and inhomogeneous cases.

2. Diffusion model of photon migration

When using a pulsed radiation source, i.e., in the process of time-resolved DOT, it is common to pay attention to the initial and middle parts of each TPSF curve [7–9]. These parts correspond to the photons with small and medium times of flight. However, it is possible to use the final part of the diffusely passed radiation as well. This part of the TPSF corresponds to late-arriving photons (LAPs) [9] that practically do not contribute to the calculation of the mean time of flight for the diffusely transmitted radiation pulse [7, 8].

Being presented as two-dimensional plots, characterising the dependence of the radiation intensity on time for different angles, the TPSFs in the homogeneous case converge into a single line [3,10], while in the inhomogeneous case they are parallel lines [3]. The type of convergence is most distinguishable in the end part of the TPSF. To confirm this assumption, using the physical model [2, 3] and the computer model [2] implemented in the graphics programming language G of the LabVIEW system-design platform and development environment for visual programming, the experimental and theoretical TPSFs were obtained for homogeneous and inhomogeneous cases.

The theoretical TPSFs, presented in this paper, were obtained numerically using the model of a drop, i.e., the radiation pulse containing a fixed initial number of photons that appears in the object near its surface and diffuses within the object, decaying exponentially and moving mainly towards its centre [2]. Such an approach that allows sufficiently precise description of experimental data for homogeneous and inhomogeneous cases (Fig. 1) is based on the solution of the radiative transfer equation [9] for a light pulse, containing a finite number of photons. According to the diffusion equation, the density of diffusing photons is described as

$$\frac{1}{c}\frac{\partial \phi(r,t)}{\partial t} - D(r)\nabla^2 \phi(r,t) + \mu_a(r)\phi(r,t) = S(r,t), \forall r \in \Omega, \quad (1)$$

where Ω is the finite spatial domain (object); $c = c_0/v_{obj}$ is the speed of light in the medium; c_0 is the speed of light in vacuum; v_{obj} is the relative refractive index of the modelled object Ω and its boundary $\partial\Omega$;

$$D(r) = \frac{1}{3[\mu_a(r) + (1-g)\mu_s(r)]}$$

is the diffusion coefficient at the position r; $\mu_a(r)$ and $\mu_s(r)$ are the absorption and scattering coefficient at the point r; g is the mean cosine of the scattering angle (the anisotropy parameter) equal for all r; and $S(r,t)$ is the photon source function, i.e., the time dependence of the number of photons introduced into the modelled object Ω at a single point q of the boundary $\partial\Omega$.
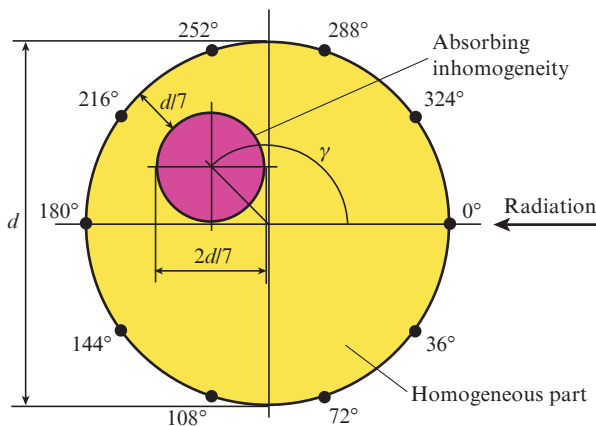

Figure 1. Schematic diagram of the studied object for the inhomogeneous case. The pulsed radiation is simulated as a drop that falls near the boundary and diffuses towards the object centre.

The majority of errors in modelling photon propagation through strongly scattering media are rather due to the boundary conditions and photon sources than to the diffusion approximation [11]. In this connection, the boundary condition of the third kind (the Robin condition) is used to describe the photon flux at all points of the boundary $\partial\Omega$ of the domain Ω, except the point q. The flux of photons, leaving the finite domain through the boundary, is equal to the flux at the boundary, multiplied by the coefficient that takes into account the reflection of light back into the object [8, 12, 13]:

$$\phi(r,t) + 2D(r)F\frac{\partial \phi(r,t)}{\partial n(r)} = 0, \ \forall r \in \partial\Omega, \ r \neq q, \quad (2)$$

where n is the direction of the outer normal to the boundary $\partial\Omega$ of the finite domain Ω at the point r;

$$F = \left(\frac{2}{1-R_0} - 1 + |\cos Q_a|^3\right)(1 - |\cos Q_a|^2)^{-1}$$

is the Fresnel reflection coefficient [13];

$$R_0 = \left(\frac{v_{obj}}{v_{med}} - 1\right)^2 \left(\frac{v_{obj}}{v_{med}} + 1\right)^{-2}, \quad Q_a = \arcsin\frac{v_{med}}{v_{obj}}$$

are the coefficients [13]; and v_{med} is the relative refractive index of the medium surrounding the object (usually it is air and, therefore, $v_{med} = 1$).

The numerical solution of Eqn (1) with the boundary condition (2) was carried out using the finite-difference method. The implicit difference scheme was constructed using a seven-point pattern. The initial approximation of the function $\phi(r,t)$ in all mesh nodes was generated with the photon source position and the injected photons number taken into account. The criterion for terminating the iteration process was either attaining the prescribed precision (fitting criterion) or time-out.

The results of the photon density simulation in the homogeneous and inhomogeneous objects with cylindrical geometry are shown in Fig. 2. The described computer simulation completely repeats the experimentally implemented physical model [2, 3]. It is a regular cylinder having the diameter $d = 68$ mm and similar height. Figure 2a shows the distribution of photons in the homogeneous case over the cross section of the modelled cylinder at the height of the source and the detector for the moment of time $t = 0.5$ ns. The absorption $\mu_a(r)$ and reduced scattering $\mu'_s(r)$ coefficients for $\forall r \in \Omega$ amount to 0.004 and 0.5 mm^{-1}, respectively. In the inhomogeneous case, for which the distribution of photons is also presented as a cross-section (Fig. 2b), in the modelled object at an angle of $\gamma = 180°$ with the axis of the incident radiation (see Fig. 1) at the depth $d/7$ an absorbing inhomogeneity with the dimension of $2d/7$ is present having the absorption coefficient 0.04 mm^{-1}. The mesh spacing in all three coordinate axes was chosen equal, $h = 0.5$ mm. The time step was $\Delta t = 1$ ps.

3. Comparison of theoretical and experimental results

Figure 3 presents the data of physical experiment [3] and the computer simulation for the homogeneous case. The relative deviation of theoretical curves from the experimental ones is $\Delta = 4.3\%$. The TPSFs are shown for the following five detector positions: 36°, 72°, 108°, 144°, and 180°. The experimental
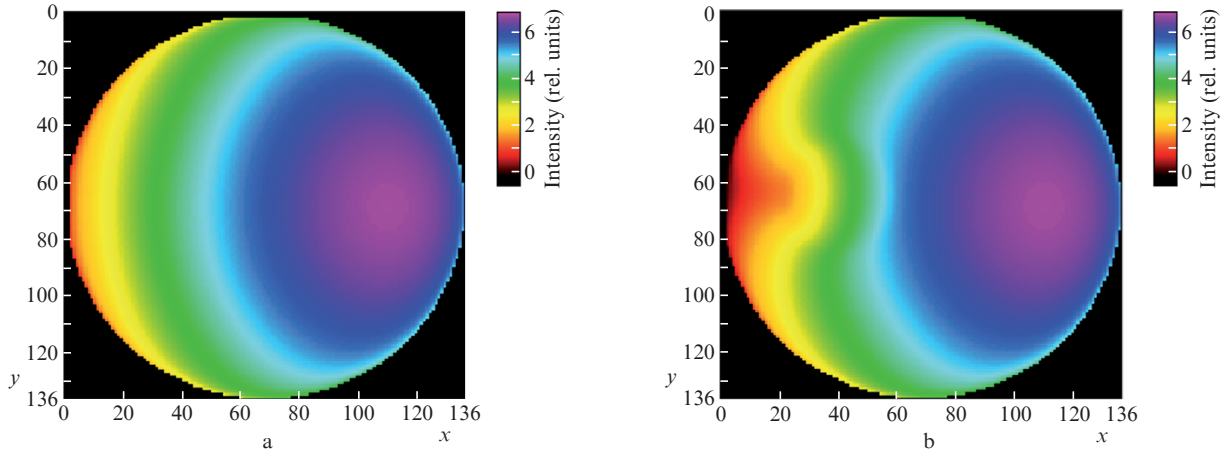
Figure 2. Distribution of photons in (a) the homogeneous and (b) inhomogeneous cylindrical object.
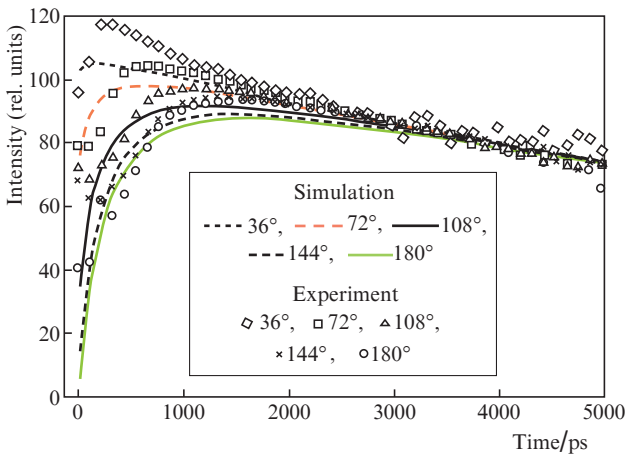

Figure 3. Comparison of results of numerical simulation and experiment (homogeneous case). The optical characteristics of the model object are similar to those in Fig. 2a.
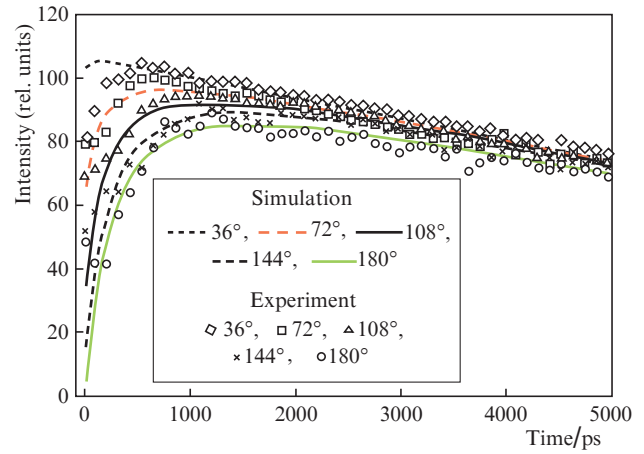

Figure 4. Comparison of results of numerical simulation and experiment (inhomogeneous case). The optical characteristics of the model object are similar to those in Fig. 2b.

and theoretical curves converge into a single line, the best agreement being attained at the end parts of the TPSFs, i.e., for the LAPs. In the inhomogeneous case (Fig. 4) the type of convergence (into parallel lines) becomes apparent only at the end part of TPSFs, too. The relative deviation is $\Delta = 3.32\%$.

In connection with the above considerations, it is proposed to simplify the three-dimensional imaging problem by using only the last part of the diffusely transmitted radiation, i.e., the LAP part of each TPSF.

Note that if we present all TPSFs for one object as a function $R(\alpha, t)$, where $\alpha = 360°/N, 2(360°/N), \ldots, 360°$ are the angles between the optical waveguides of the radiation source and the detector; N is the number of detectors; and $t = n, 2n, \ldots, T$ are the discrete time values separated by the step n, and visualise them as a three-dimensional surface in the Cartesian coordinate system, then in the homogenous case we get a saddle function smoothly transforming into a plane (Fig. 5a), while in the inhomogeneous case (absorbing inhomogeneity) the analogous surface (Fig. 5b) demonstrates a valley in the part, corresponding to the TPSF recorded by the detectors closest to the inhomogeneity [3, 7]. The advantage of this approach is that in all asymmetric cases it allows direct real-time detection of the inhomogeneity without solving the inverse problem. However, at the present stage the calcula-

tions are applicable only to sufficiently large and strongly absorbing inhomogeneities. If the dimension of the inhomogeneity is smaller than $0.05d$ and it is located close enough to the centre of the object (at the distance smaller than $0.4d$), then the valley in the three-dimensional surface will be insignificant (the relative deviation from the homogeneous case smaller than 1%).

4. Three-dimensional visualisation in a cylindrical coordinate system

In connection with low informativity of the classical two-dimensional representation of time dependences of the radiation intensity (Figs 3 and 4) and insufficient informativity of the three-dimensional representation, described above (Fig. 5), we propose a visualisation method based on a conformal transformation. The method consists in the preliminary processing of the function $R(\alpha, t)$ followed by its representation in the form of three-dimensional surfaces in a cylindrical coordinate system. For such a representation of the TPSF in the homogeneous case the distance from the generatrix of the cylindrical surface to its directrix (the cylinder axis) is constant. Any deviations from this distance (the unit radius) are characteristic only for inhomogeneous cases. Due to the
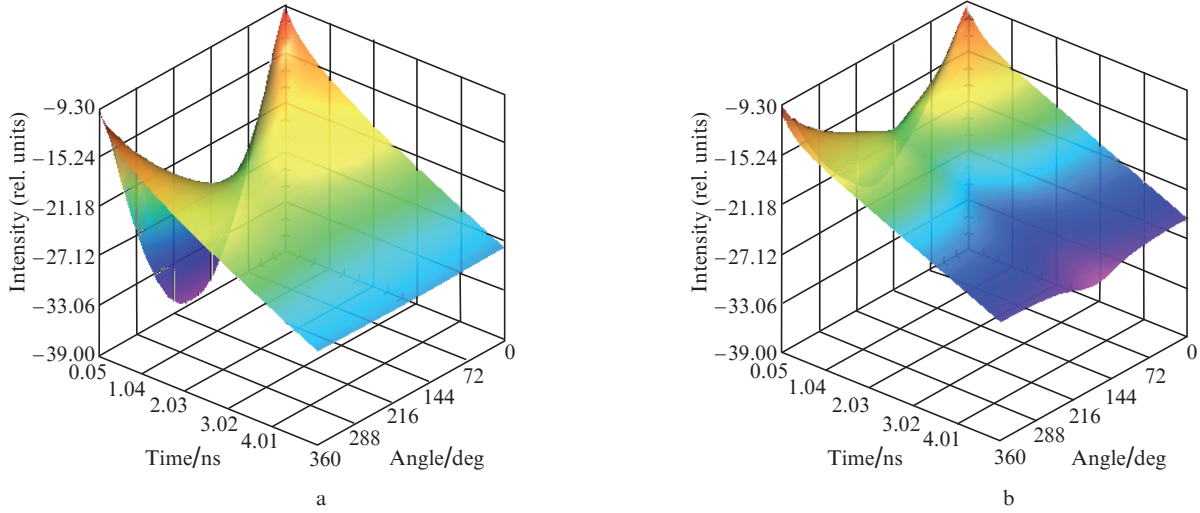
Figure 5. Three-dimensional representation of the TPSF temporal dependences in the Cartesian coordinate system for (a) the homogeneous and (b) inhomogeneous case. The surfaces are plotted using the theoretical TPSFs, presented in Figs 3 and 4.

use of the cylindrical system the inhomogeneous case will be not simply distinguishable from the homogeneous one. The angle between the axis of the incident radiation and the direction towards the detector, nearest to the inhomogeneity will be detectable and, therefore, for spherical and cylindrical objects the approximate position of inhomogeneity will be detectable.

To visualise late-arriving photons in all TPSFs the initial parts, corresponding to the early arrived photons, and the middle parts, corresponding to photons with medium time of light, are removed, i.e., the tail parts of the TPSFs are found by the logical subtraction of two functions:

$$R_\text{p}(\alpha, t_1) = R(\alpha, t)\backslash R(\alpha, t_2),$$

where $t_2 = n, 2n, \ldots, T_\text{isot}$; $t_3 = T_\text{isot}, T_\text{isot} + n, \ldots, T$; T_isot is the minimal time interval from the moment of pulse incidence on the object to the moment of reaching the diffusion centre, when all lines can be considered to be parallel within the measurement error; and the sign '\' denotes the logical subtraction. After the logical subtraction of functions, the normalisation of $R_\text{p}(\alpha, t_3)$ with respect to $R_\text{p}(360°/N, t_3)$ is carried out, which means the division of the TPSFs for all angles by the TPSF for the minimal angle:

$$R_\text{n}(\alpha, t_3) = \frac{R_\text{p}(\alpha, t_3)}{R_\text{p}(360°/N, t_3)},$$

each TPSF becoming approximated by a straight line.

Based on the function $R_\text{n}(\alpha, t_3)$ the etalon function $R_\text{st}(\alpha, t_3)$ is created, in which the TPSFs for all angles are equal to the TPSF with the angle $\alpha = 360°/N$:

$$R_\text{st}(\alpha, t_3) = R_\text{n}(360°/N, t_3).$$

With the additional transformation coefficient K taken into account, the function $R_\text{n}(\alpha, t_3)$ is modified (amplification, curvature reduction) in the following way:

$$R_K(\alpha, t_3) = \begin{cases} 1, & R_\text{n}(\alpha, t_3) = 1, \\ 1 + [R_\text{n}(\alpha, t_3) - 1]K, & R_\text{n}(\alpha, t_3) \neq 1. \end{cases} \quad (3)$$

The coefficient K is specified by the user and can be any real number except zero.

Obviously, the function $R_\text{st}(\alpha, t_3)$ and also (in the homogeneous case) the function $R_K(\alpha, t_3)$ will be equal to one for any α, t_3, and K from the admitted region. To visualise them as three-dimensional surfaces in the cylindrical coordinate system, let us transform the coordinates from Cartesian to cylindrical ones:

$$q = \sqrt{\alpha^2 + t_3^2}, \quad \psi = \arctan\frac{\alpha}{t_3}. \quad (4)$$

To provide the correctness of the transformation, the angles $\alpha = 360°/N, 2(360°/N), \ldots, 360°$ are expressed in radians instead of angular degrees. As a result of mapping, the functions $R_\text{st}^*(q, \psi)$ and $R_K^*(q, \psi)$ are obtained

$$R_\text{st}(\alpha, t_3) \rightarrow R_\text{st}^*(q, \psi), \quad (5)$$

$$R_K(\alpha, t_3) \rightarrow R_K^*(q, \psi), \quad (6)$$

which represent two exactly coincident cylindrical surfaces (like those of regular circular cylinders).

In the inhomogeneous case the function $R_K(\alpha, t_3)$ will be unambiguously equal to one only if $\alpha = 360°/N$ and any admissible t_3. For other values of α, i.e., for other TPSFs the value of the function $R_K(\alpha, t_3)$ will differ from one upward or downward depending on the inhomogeneity type (absorbing, scattering), its location, size and the value of the coefficient K. The application of the transformation $R_K(\alpha, t_3)$ to the function (6) using Eqn (4) yields an irregular cylindrical surface, and from the character of its distortion with respect to a regular circular cylindrical surface $R_\text{st}^*(q, \psi)$ one can draw conclusions about the size and location of the inhomogeneity.

5. Results and discussion

The proposed method of preliminary processing of the set of TPSFs followed by their visualisation in the form of two three-dimensional surfaces in the cylindrical system of coordi-
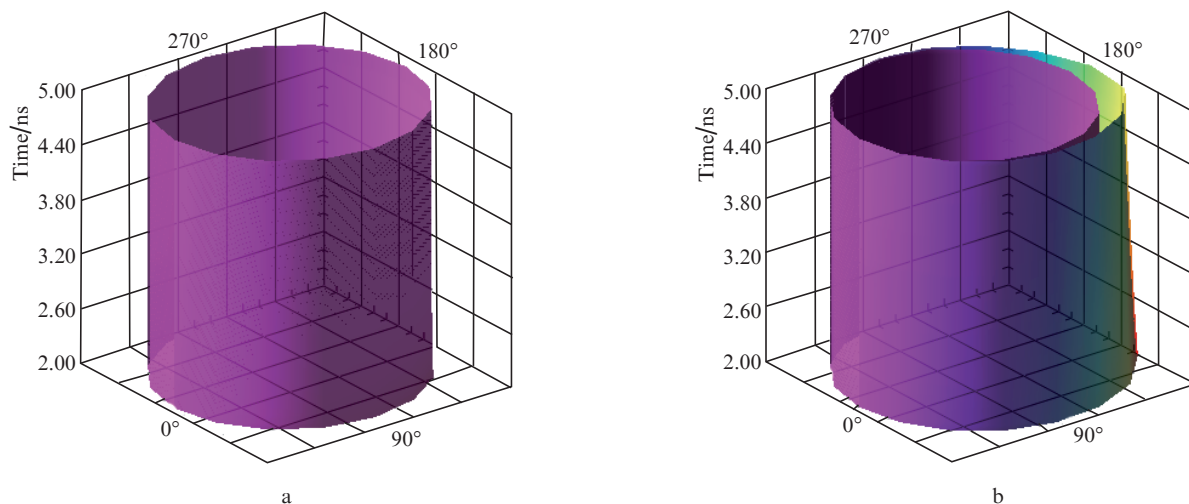
Figure 6. Three-dimensional representation of LAP for (a) the homogeneous and (b) inhomogeneous case for $K = 3$. The surfaces are plotted using the theoretical TPSFs, presented in Figs 3 and 4.

nates was implemented as a special-purpose software product in the LabVIEW environment [14]. The results of its operation for the homogeneous and inhomogeneous case are shown in Fig. 6. In the inhomogeneous case the surfaces are presented using the coefficient $K = 3$. It is seen that at $K > 1$ the distorted part of the cylindrical surface is amplified by K times and sticks out of the regular circular cylindrical surface. In other words, the etalon cylindrical surface provides a lower boundary that separates the homogeneous case from all inhomogeneous ones, thus enhancing the efficiency of inhomogeneity direct detection.

With the aim of additional estimation of the proposed method, we compared the results of two kinds of three-dimensional representation of the TPSF time dependences (Fig. 7). In the case shown in Figs 7a and 7b the model object was used, for which the distribution of photons is shown in Fig. 2b, but with the inhomogeneity absorption coefficient being equal to 0.005 mm^{-1}. For the cylindrical surfaces of the inhomogeneous case (Figs 7c and 7d) the absorption coefficient in the inhomogeneity of this model object was doubled. In the case shown in Figs 7e and 7f the absorption coefficient was doubled again. In the conformal transformation into the cylindrical coordinate system the value $K = -7$ was used.

From Fig. 7 it follows that the recalculation of the cylindrical surface wall distortion using Eqn (3) and its visualisation against the background of the etalon surface allows the detection of the inhomogeneity presence without solving the inverse problem. It is also seen that for $K < -1$ the curved part of the inhomogeneous cylindrical surface is enhanced by K times and located inside the etalon surface. For absorbing inhomogeneities it is more preferable to use $K < -1$. Obviously, for a scattering inhomogeneity the influence of K is opposite [4], i.e., for $K > 1$ the scattering inhomogeneity is mapped inwards the etalon surface and for $K < -1$ – outwards the etalon surface.

Real biological objects possess a complex structure of the inhomogeneity distribution, thus making it reasonable to estimate the efficiency of the proposed method in such cases. As a modelled object we continue to use the cylinder, similar in its geometric parameters to the one used in the physical experiments (Fig. 1). The fact that the inhomogeneity has the diam-

eter $2d/7$, i.e., about 20 mm, generally corresponds to many clinical cases, since the region of angiogenesis that surrounds a real tumour a few millimetres in diameter has the size of a few centimetres [15]. Both the tumour itself and the region of pathological formation of new blood vessels (angiogenesis) will be modelled as one distinctly expressed inhomogeneity with diffuse boundaries. Both the healthy tissue and the inhomogeneity will be considered as randomly inhomogeneous with respect to the value of $\mu_a(r)$ and strongly scattering media [8, 16], but the mean value of the absorption coefficient for the tumour and the region of new blood vessels formation will be taken to be considerably higher than that for the healthy tissue [16, 17]. Figure 8a presents the fluctuations of $\mu_a(r)$ in the cross section of the modelled object at the height of the source and the detectors. The mean value of the absorption coefficient for the inhomogeneous part (the tumour and the angiogenesis region) was taken equal to 0.01 mm^{-1}, for healthy tissue 0.0045 mm^{-1} [16]. The scattering coefficient $\mu_s'(r)$ for the modelled object was constant (Fig. 8b) and equal to 1 mm^{-1} [16].

The TPSFs obtained as a result of modelling are presented in Fig. 9. From the figure it follows that the randomly inhomogeneous structure of the healthy tissue affected all detectors and, therefore, the shape of all TPSFs in a nearly similar way. The effect appeared to consist in a general reduction of the time-resolved signal intensity and, therefore, was not distinctly observable. But the region with the mean absorption coefficient value 0.01 mm^{-1}, i.e., the inhomogeneity to be detected, essentially changed the shape of some TPSFs, particularly, their parts corresponding to LAPs (Table 1). The nearer the detector to the inhomogeneity, the stronger the decrease in the intensity of the time-resolved signal at this detector.

Figure 10 presents the three-dimensional surfaces in the cylindrical coordinate system, obtained as a result of processing the TPSF (Fig. 9) by means of the proposed method. The distorted part of the cylindrical surface clearly indicates the presence of the absorbing inhomogeneity at the angle $\gamma \approx 180°$ to the incident radiation axis. The fact that the distortion appeared in several adjacent TPSFs (separated by the angle 36°) provides an indirect evidence of the size and approximate depth of the inhomogeneity.
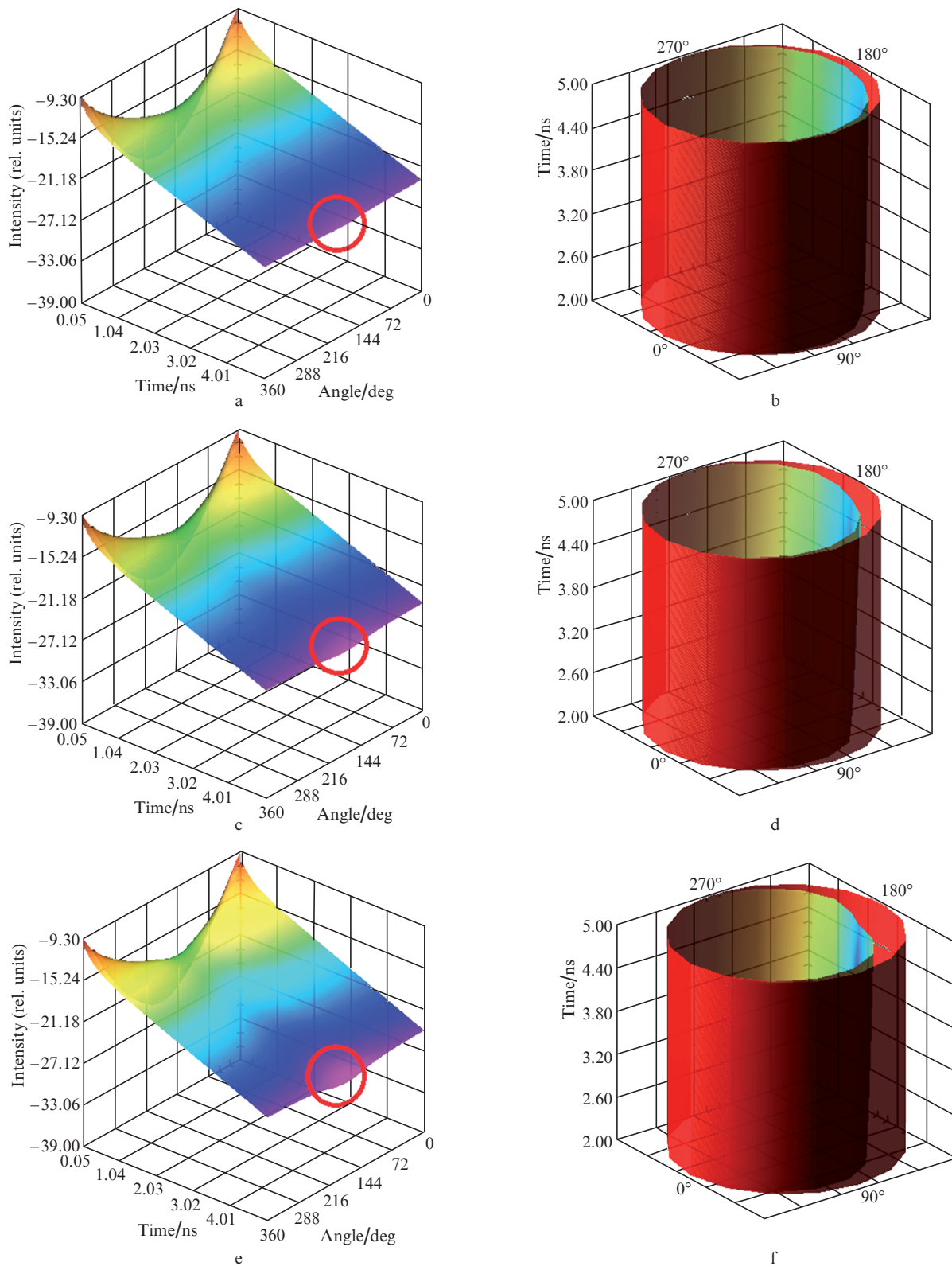
Figure 7. (a, c, e) Three-dimensional representation of the TPSF in the Cartesian coordinate system and (b, d, f) the corresponding mapping in the cylindrical system for different values of $\mu_a(r)$ for the absorbing inhomogeneity (see text).

6. Conclusions

The present paper describes the method for detecting inhomogeneities in diffuse optical tomography by three-dimensional representation of the tail part of TPSFs in a cylindrical coordinate system. In all asymmetric cases the method allows real-time direct detection of an absorbing inhomogeneity in cylindrical and spherical objects, avoiding the solution of the inverse problem. In contrast to the three-dimensional representation in the Cartesian coordinates, this representation
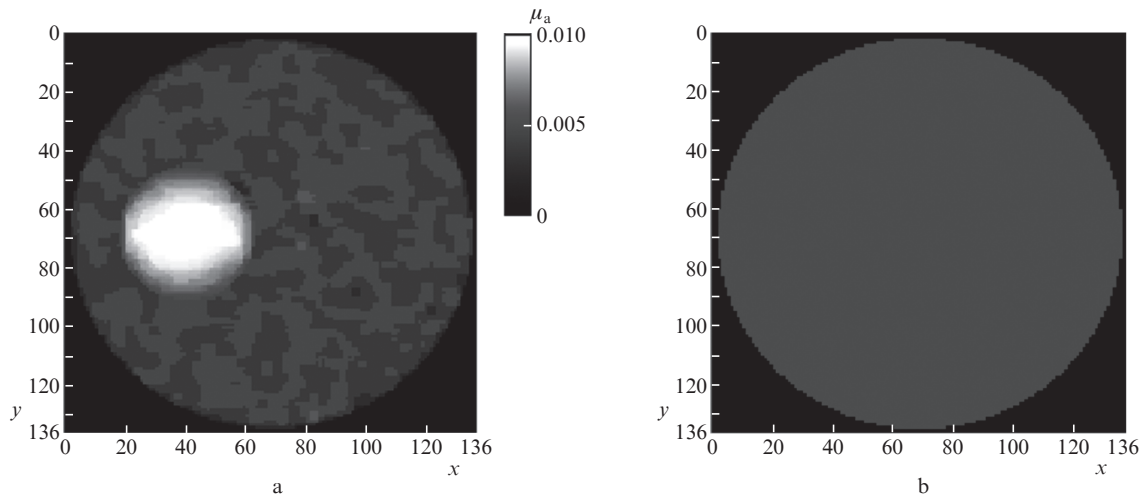
Figure 8. Spatial distribution of $\mu_a(r)$ and $\mu_s'(r)$ over the cross section of the modelled randomly inhomogeneous cylindrical object.
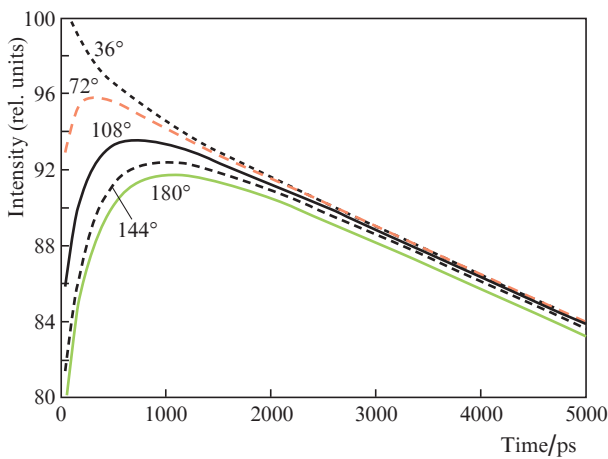

Figure 9. Computer simulation of the TPSF for the cylindrical object randomly inhomogeneous with respect to the values of $\mu_a(r)$ in the cylindrical object.
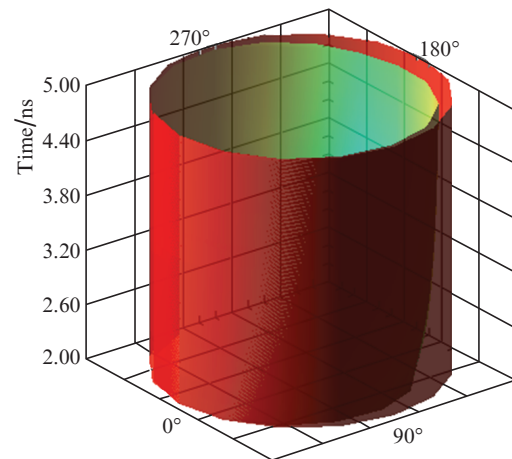

Figure 10. Three-dimensional representation of LAPs for randomly inhomogeneous cylindrical object for $K = -5$.

Table 1. Relative deviation of the mean intensity of the time-resolved signal at all detectors from the mean intensity on the detector at the minimal angle (36°), Δ being calculated for LAPs only.

Detector location α/deg	Relative deviation Δ (%)
36	0
72	0.09
108	0.62
144	1.83
180	3.53
216	1.78
252	0.58
288	0.08
324	0.01

with the mapping coefficients correctly chosen, $K < -1$, possesses clearly expressed boundaries, i.e., the surface and the directrix of the etalon cylindrical surface, between which all possible cases of inhomogeneity are located.

The proposed method can be used in time-resolved DOT for rapid detection of haematomas, tumours, cists, etc., in mammographic studies and diagnostics of brain structures. Since the conformal transformations of TPSFs in the cylindrical coordinate system does not require high-performance cal-

culations, it can be used to detect the pathology inside the studied object in real time, after which one can reconstruct the image using the known techniques [7, 8, 12, 13, 16], or use an alternative diagnostic method.

Further efforts will be focused at considering the objects with the structure randomly inhomogeneous with respect to $\mu_s(r)$ and at solving the inverse problem with the use of LAPs.

References

1. Zimnyakov D.A., Tuchin V.V. *Kvantovaya Elektron.*, **32** (10), 849 (2002) [*Quantum Electron.*, **32** (10), 849 (2002)].
2. Proskurin S.G., Potlov A.Y. *Photon. Las. Med.*, **2** (2), 139 (2013).
3. Proskurin S.G. *Kvantovaya Elektron.*, **41** (5), 402 (2011) [*Quantum Electron.*, **41** (5), 402 (2011)].
4. Abascal J., Arridge S., Atkinson D., Shindmes R., Fabrizi L., DeLucia M., Horesh L., Bayford R., Holder D. *Neuroimage*, **43**, 258 (2008).

5. Fiks I.I. *Vestnik Nizhegorodskogo universiteta im. N.I. Lobachevskogo*, **4** (1), 190 (2011).
6. Proskurin S.G., Potlov A.Yu., Frolov S.V. *Med. Tekh.*, **6** (276), 1 (2012).
7. Tretyakov E.V., Shuvalov V.V., Shutov I.V. *Kvantovaya Elektron.*, **31** (11), 1095 (2001) [*Quantum Electron.*, **31** (11), 1095 (2001)].
8. Konovalov A.B., Vlasov V.V., Kalintsev A.G., Kravtsenyuk O.V., Lyubimov V.V. *Kvantovaya Elektron.*, **36** (11), 1048 (2006) [*Quantum Electron.*, **36** (11), 1048 (2006)].
9. Patterson M., Chance B., Wilson B. *Appl. Opt.*, **28**, 2331 (1989).
10. Arridge S., Cope M., Delpy D. *Phys. Med. Biol.*, **37**, 1531 (1992).
11. Durian D., Rudnick J. *J. Opt. Soc. Am. A.*, **16**, 4 (1999).
12. Schweiger M., Arridge S. *Phys. Med. Biol.*, **44**, 1699 (1999).
13. Dehghani H., Srinivasan S., Pogue B., Gibson A. *Phil. Trans. R. Soc. A*, **367**, 3073 (2009).
14. Proskurin S.G., Frolov S.V., Potlov A.Yu. Svid. o gos. reg. programmy dlya EVM v FIPS No. 2013611012, 2013 [Certificate of State Registration of a Computer Program at the Federal Institute of Industrial Property No. 2013611012, 2013].
15. Naumov G., Bender E., Zurakowski D., Kang S-Y., et al. *J. Natl. Cancer Inst.*, **98** (5), 316 (2006).
16. Konovalov A.B., Vlasov V.V., Mogilenskikh D.V., Kravtsenyuk O.V., Lyubimov V.V. *Kvantovaya Elektron.*, **38** (6), 588 (2008) [*Quantum Electron.*, **38** (6), 588 (2008)].
17. Roggan A., Friebel M., Dorschel K., Hahn A., Muller G. *J. Biomed. Opt.*, **4** (1), 36 (1999).